

# Classical treatment of ion-H<sub>2</sub>O collisions with a three-center model potential

Clara Illescas,<sup>1</sup> L. F. Errea,<sup>1</sup> L. Méndez,<sup>1</sup> B. Pons,<sup>2</sup> I. Rabadán,<sup>1</sup> and A. Riera<sup>1</sup>

<sup>1</sup>*Laboratorio Asociado al CIEMAT de Física Atómica y Molecular en Plasmas de Fusión, Departamento de Química, módulo 13, Universidad Autónoma de Madrid, Cantoblanco, E-28049 Madrid, Spain*

<sup>2</sup>*CELIA, Université de Bordeaux I-CNRS-CEA, 351 Cours de la Libération, F-33405 Talence, France*

(Received 17 January 2011; published 18 May 2011)

We present calculations of cross sections for one- and two-electron processes in collisions of H<sup>+</sup>, He<sup>2+</sup>, and C<sup>6+</sup> with water molecules in the framework of the Franck-Condon approximation. We employ an independent-electron method and a classical trajectory Monte Carlo approach. Anisotropy effects related to the structure of the target are explicitly incorporated by using a three-center model potential to describe the electron-H<sub>2</sub>O<sup>+</sup> interaction. We derive scaling laws with respect to the projectile charge. We also estimate cross sections for molecular fragmentation subsequent to electron removal.

DOI: [10.1103/PhysRevA.83.052704](https://doi.org/10.1103/PhysRevA.83.052704)

PACS number(s): 34.50.Gb, 34.70.+e, 82.39.Jn

## I. INTRODUCTION

Ion-beam cancer therapy has been shown to be a valuable alternative to x- or  $\gamma$ -ray radiotherapy (see [1,2] for reviews). The use of this technique started in 1954 at the Lawrence Berkeley National Laboratory (United States) [3]; since then, several thousands of patients have been treated with proton beams in several installations and with carbon ion beams at Chiba (Japan) [4] and Darmstadt (Germany) [5]. Compared to conventional photon radiation, the use of ion beams has several advantages: it allows access to deeply seated tumors, and the lethal tumor dose is raised while the surrounding healthy tissue remains unaffected. Physicists and biologists can measure and/or compute the intensity, penetration depth, and lethal dose of the ion beams [6–9]. Nevertheless, the mechanisms responsible for the dissociation of the DNA chain, which subsequently lead to cell death, remain quite obscure. Some experiments have therefore considered, in the last few years, collisions of multicharged ions with DNA bases to shed light on the fragmentation processes (see, e.g., [10]). Further fundamental studies, especially on the theoretical side, are required since the underlying mechanisms are intricate.

On the other hand, electron-DNA experiments [11] have shown that collisions of relatively slow electrons (with energy of about 10 eV) can lead to the breakdown of DNA through a mechanism that involves the formation of intermediate resonant states. Therefore, processes that lead to the production of electrons are also relevant to understanding biological damage and ion therapy. In this respect, electron emission in collisions of ions with water provides the most significant source of electrons in the interaction of ion beams with the cell. Although several experiments [12–14] have provided detailed information on ionizing proton-water collisions, data are scarce for multicharged ion impact. Furthermore, beyond purely ionizing reactions, all other processes, such as elastic scattering, excitation, and charge exchange in ion-H<sub>2</sub>O collisions, are amenable to target fragmentation (and subsequent biological effects). Therefore, these processes must also be explicitly considered to reliably simulate the passage of charged particles in biological (cell) environments [15,16].

Previous theoretical works aimed at filling in the collisional database of interest for radiation damage. Nevertheless, most

of those works focused on H<sup>+</sup> + H<sub>2</sub>O collisions and employed perturbative methods [17], such as the continuum-distorted-wave-eikonal-initial-state (CDWEIS) [18–20] and first-order Born (FB) approximations [21], which are, in general, useful at impact energies  $E$  greater than 100 keV/amu. In a previous work [22], we employed the classical trajectory Monte Carlo (CTMC) method to evaluate single-ionization and single-capture cross sections in H<sup>+</sup> + H<sub>2</sub>O collisions at energies  $25 \text{ keV} < E < 5 \text{ MeV}$ . We used the independent-particle method (IPM) [23–25], where the electrons are treated as independent particles that follow trajectories obtained by solving the Hamilton equations with a one-center (isotropic) model potential to describe the interaction between the active electron and the molecular core. Recently, Lüdde *et al.* [26] applied the basis-set-generator method (BGM) to H<sup>+</sup> + H<sub>2</sub>O collisions, beyond the isotropic electron-core approximation; they have reported electron production and net capture cross sections in good agreement with experiment.

With respect to water collisions with multicharged ions, He<sup>2+</sup> + H<sub>2</sub>O collisions have been considered in Refs. [27] and [28] in the framework of FB and classical models, respectively. Comparison with experimental data showed acceptable, but not very satisfactory, agreement. In spite of the interest in C<sup>6+</sup> + H<sub>2</sub>O collisions in ion-based cancer therapy, only CDWEIS [29] and FB [30] calculations of the total ionization cross section have been reported so far, together with a single experimental point at 6 MeV/amu [29].

In this work, we employ an improved CTMC model to calculate cross sections for single-ionization, single-capture, and two-electron processes (transfer ionization, double capture, and double ionization) in H<sup>+</sup>, He<sup>2+</sup>, and C<sup>6+</sup> + H<sub>2</sub>O collisions in the impact-energy range  $20 \leq E \leq 10\,000 \text{ keV/amu}$ . We largely encompass the intermediate- and high-impact-energy regimes of interest for therapy applications. The basic assumptions of our treatment, together with preliminary results, were presented at the Radiation Damage (RADAM) Conference of 2008 (see [31]). As in most of the available calculations, our treatment is based on assuming that the electrons are independent, so that each electron moves in an effective field created by the nuclei and the remaining electrons. In practice, this involves the use of electron-core effective potentials. In contrast with previous calculations,

which employed one-center (isotropic) potentials [22], we presently use a three-center model potential to describe the interaction of the active electron with the  $\text{H}_2\text{O}^+$  core; this allows us to explicitly consider the anisotropy of the molecular target. In this respect, it is noteworthy that relevant anisotropy effects have been detected in calculations of both  $\text{H}^+$ - and  $e$ - $\text{H}_2\text{O}$  collisions (see, e.g., [26,32]). The evaluation of inelastic probabilities for the physical many-electron system, in terms of the mono-electronic ones resulting from the model potential calculations, is performed by means of the independent-event model (IEVM) [33–36], which has been found [31,37] to be more adequate than the usual IPM for multielectronic targets.

This paper is organized as follows: In Sec. II, we summarize the basic assumptions of our CTMC approach, emphasizing the description of the initial electron densities associated with the molecular orbitals; we present our results for  $\text{H}^+ + \text{H}_2\text{O}$  collisions and compare them to the large amount of both experimental and theoretical existing data in Sec. III. Sections IV and V contain our results for  $\text{He}^{2+}$  and  $\text{C}^{6+}$  ion impacts, respectively. Useful scaling relations with respect to the projectile charge and the impact energy are presented in Sec. VI, where fragmentation cross sections are further displayed in the case of  $\text{H}^+ + \text{H}_2\text{O}$  collisions. Finally, conclusions and perspectives issued from the present work are given in Sec. VII. Atomic units are used throughout unless otherwise indicated.

## II. IMPACT-PARAMETER-CTMC APPROACH

Since we consider relatively high collision energies, we apply the Franck-Condon approximation, where the nuclei of the  $\text{H}_2\text{O}$  molecule remain at their equilibrium positions during the collision. Furthermore, we employ the impact-parameter approximation [38] in which the relative ion-molecule motion is described by straight-line trajectories  $\mathbf{R}(t) = \mathbf{b} + \mathbf{v}t$ , where  $\mathbf{R}$  is the ion position vector with respect to the origin of coordinates, placed on the oxygen nucleus of the target molecule,  $\mathbf{b}$  is the impact parameter, and  $\mathbf{v}$  is the constant relative velocity.

### A. Electronic motion of the active electron: Initial distributions and mono-electronic probabilities

As stated in the Introduction, we consider that each of the 10 electrons involved in bare-ion- $\text{H}_2\text{O}$  collisions evolves independently, subject to the mean field created by the nuclei and the other nine electrons. Furthermore, we assume that two electrons are too deeply bound to the O nucleus in the  $1a_1$  molecular orbital (MO) of  $\text{H}_2\text{O}$  to significantly participate in the collision dynamics. We thus explicitly consider the dynamics of the eight electrons initially located in the four outermost MOs of  $\text{H}_2\text{O}$ , with symmetries  $2a_1$ ,  $1b_2$ ,  $3a_1$ , and  $1b_1$ . In the framework of mean-field theory, the four MOs  $\phi_i$  (with  $i = 1, \dots, 4$ ) and associated energies  $\epsilon_i$  can be accurately reproduced using a three-center model potential [31] that has the form

$$V_{\text{mod}}(\mathbf{r}) = V_{\text{O}}(r_{\text{O}}) + V_{\text{H}}(r_{\text{H1}}) + V_{\text{H}}(r_{\text{H2}}), \quad (1)$$

with

$$\begin{aligned} V_{\text{O}}(r_{\text{O}}) &= -\frac{8 - N_{\text{O}}}{r_{\text{O}}} - \frac{N_{\text{O}}}{r_{\text{O}}}(1 + \alpha_{\text{O}}r_{\text{O}})\exp(-2\alpha_{\text{O}}r_{\text{O}}), \\ V_{\text{H}}(r_{\text{H}}) &= -\frac{1 - N_{\text{H}}}{r_{\text{H}}} - \frac{N_{\text{H}}}{r_{\text{H}}}(1 + \alpha_{\text{H}}r_{\text{H}})\exp(-2\alpha_{\text{H}}r_{\text{H}}), \end{aligned} \quad (2)$$

where  $r_{\text{O}}$ ,  $r_{\text{H1}}$ , and  $r_{\text{H2}}$  are the electron distances to the three target nuclei. To determine the parameters [ $N_{\text{O}} = 7.1$ ,  $N_{\text{H}} = (9 - N_{\text{O}})/2$ ,  $\alpha_{\text{O}} = 1.500a_0$ ,  $\alpha_{\text{H}} = 0.665a_0$ ], we have solved the Schrödinger equation  $H_0\phi_i = (p^2/2 + V_{\text{mod}})\phi_i = \epsilon_i\phi_i$  by expanding  $\phi_i$  in a large Gaussian-type orbital (GTO) basis (see [39]). The values of the parameters are then obtained by minimizing the differences  $|\epsilon_i - \epsilon_i^{\text{SCF}}|$ , where  $\epsilon_i^{\text{SCF}}$  are the self-consistent field (SCF) energies of the valence MOs of  $\text{H}_2\text{O}$  obtained in the same GTO basis set. In practice, we obtained  $\max\{|\epsilon_i^0 - \epsilon_i^{\text{SCF}}|, i = 1, \dots, 4\} < 10^{-3}$  a.u.

For each of the eight electrons that are considered in the collision dynamics, the CTMC procedure [40] consists of discretizing the phase-space distribution  $\rho_i(\mathbf{r}, \mathbf{p}, t)$  in terms of  $N$  independent trajectories  $\{\mathbf{r}_j(t), \mathbf{p}_j(t)\}$  according to

$$\rho_i(\mathbf{r}, \mathbf{p}, t) = \frac{1}{N} \sum_{j=1}^N \delta(\mathbf{r} - \mathbf{r}_j(t)) \delta(\mathbf{p} - \mathbf{p}_j(t)). \quad (3)$$

Inserting this discretized  $\rho_i(\mathbf{r}, \mathbf{p}, t)$  in the Liouville equation  $\partial\rho_i/\partial t = -\{\rho_i, H\}$ , where  $H = H_0 - Z_P r_P^{-1}$  is the total collision Hamiltonian with  $Z_P$  being the projectile charge and  $r_P$  being the electron-projectile distance, we obtain the Hamilton equations

$$\begin{aligned} \frac{\partial \mathbf{r}_j}{\partial t} &= \mathbf{p}_j, \\ \frac{\partial \mathbf{p}_j}{\partial t} &= -\nabla_{\mathbf{r}_j}(V_{\text{mod}} - Z_P r_P^{-1}), \end{aligned} \quad (4)$$

which monitor the temporal evolution of the  $j$ th trajectory among the set of  $N$  independent ones.

To build up the  $\rho_i(\mathbf{r}, \mathbf{p}, t = -\infty)$  distributions, we have worked by analogy with the central potential case [41], using five random parameters. In practice, the  $t \rightarrow -\infty$  condition is approached by setting  $Z_P = 0$  in (4), and the initial phase-space conditions are established in spherical coordinates assuming that the electron is located at the perihelion of an elliptic orbit with  $\mathbf{r}_j \perp \mathbf{p}_j$  at fixed  $t$ . Thus, the five random parameters consist of (i)  $\cos\theta_r$  and (ii)  $\phi_r$  that define the orientation of the orbit in coordinate space; (iii) the value of  $\beta$ , with  $0 \leq \beta \leq 1$ , which yields the perihelion radius  $r = \frac{r_{\text{max}}}{2}(1 + \sqrt{1 - \beta})$ , where  $r_{\text{max}}$  is the maximum value of  $r$  that is obtained by solving numerically the nonlinear equation  $V_{\text{mod}}(r_{\text{max}}, \theta_r, \phi_r) - \epsilon_i = 0$ ; (iv) the azimuthal angle  $\phi_p$  of the momentum vector; and (v)  $\Delta t$ , the time interval over which the Hamilton equations (4), with  $Z_P = 0$ , have to be propagated until the distribution becomes time independent, given that the trajectories are not elliptical in the three-center  $V_{\text{mod}}$  potential.

As an illustration of the initial distributions generated by our method, we compare in Fig. 1 the classical and quantal radial distributions obtained using the three-center model potential of Eq. (1) for the four molecular orbitals considered in this work. As can be observed, the agreement is satisfactory over the

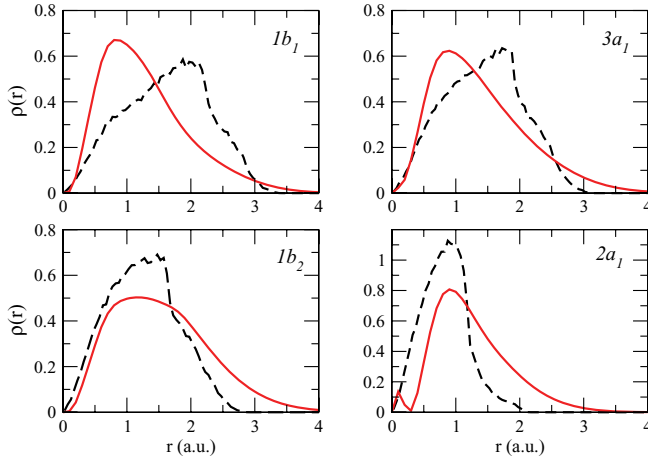


FIG. 1. (Color online) Quantal (solid lines) and classical (dashed lines) initial distributions  $\rho(r)$  as functions of  $r$  for the four valence molecular orbitals of the H<sub>2</sub>O molecule.

whole  $r$  range; the classical densities are spread out in position space similarly to those that have been obtained solving the Schrödinger equation and using a large GTO basis. Figure 2 shows the classical and quantal spatial densities associated with the  $2a_1$ ,  $3a_1$ , and  $1b_2$  MOs in the XZ plane of H<sub>2</sub>O;  $\hat{x}$  corresponds to the direction between the two H atoms and  $\hat{z} \perp \hat{x}$ . In fact, the planar classical densities correspond to the fraction of electrons that initially lie within the slab  $|y| < 0.15a_0$ , where  $y$  corresponds to the transverse direction with respect to the XZ molecular plane. In order to gauge the improvement inherent to the  $V_{\text{mod}}$  description of H<sub>2</sub>O,

we also report in Fig. 2 the classical densities issued from a monocentric (central) description of the molecule in terms of an effective charge potential  $-Z_{\text{eff}}r^{-1}$ , with  $Z_{\text{eff}} = \sqrt{-8\epsilon_i}$  (see [22]). Although any classical description inevitably fails to reproduce the nodal structure of the quantal densities, we see in Fig. 2 that the three-center model potential description allows us to better describe the electron delocalization over the three nuclei. In addition, the three-center classical densities concentrate more on the molecular plane than those obtained by means of the one-center treatment (note the different scale employed for the plots of the one-center distributions), as in the quantal description. We notice in Fig. 2 that the electron density of the  $3a_1$  MO is well described by means of the classical  $V_{\text{mod}}$  treatment. The same happens for the  $1b_1$  MO, which is not displayed in Fig. 2 because  $(x, z)$  corresponds to its nodal plane. These are positive features since the electrons should be preferentially pulled out, at low and intermediate  $E$ , from these two MOs, with the smallest ionization potentials. We shall verify this in the next section.

Once the initial distributions are generated, the Hamilton equations (4) are integrated up to the time  $t_{\text{max}} = 500/v$ , when the one-electron ionization and capture probabilities are defined, for each of the four MOs ( $i = 1, \dots, 4$ ), according to

$$p_i^{\text{ion}} = \frac{N_i^{\text{ion}}}{N}, \quad p_i^{\text{cap}} = \frac{N_i^{\text{cap}}}{N}, \quad (5)$$

where  $N_i^{\text{ion}}$  is the number of trajectories leading to ionization (those with positive energy with respect to both projectile and target at  $t_{\text{max}}$ ) and  $N_i^{\text{cap}}$  is the number of trajectories leading to electron capture (those with negative energy with respect to

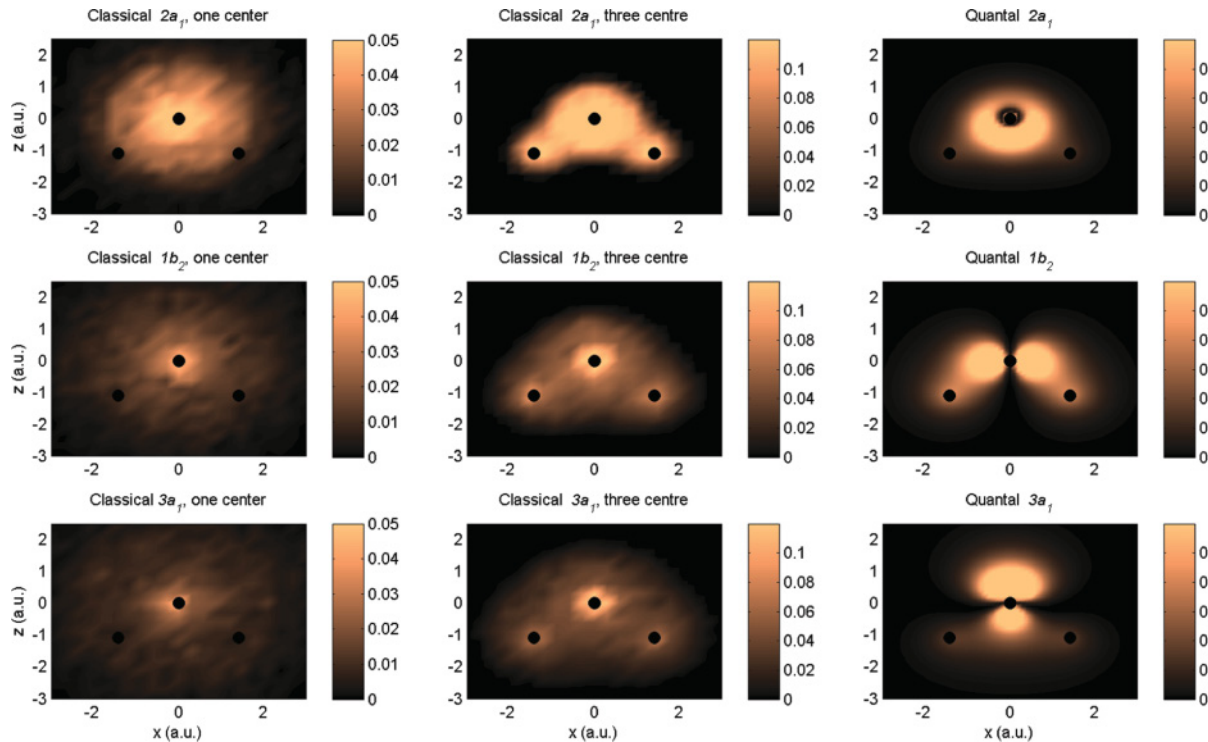


FIG. 2. (Color online) Contour plots of the quantal distributions on the molecular plane ( $y = 0$ , right) and the classical distributions for those trajectories with  $|y| < 0.15a_0$  (left, monocentric potential; middle, tricentric potential) for the  $2a_1$ ,  $1b_2$ , and  $3a_1$  MOs. The color scale of each panel is also shown.

the projectile at  $t_{\max}$ ). The probability that the electron remains bound to the target (either in the initial or in an excited state) is therefore  $p_i^{\text{el}} = 1 - p_i^{\text{ion}} - p_i^{\text{cap}}$ .

### B. Multielectronic probabilities

In order to relate the one-electron probabilities of Eq. (5) to those of the physical many-electron system, one can apply the IPM, as in our previous calculation [22], where the probabilities for single ionization (SI) and single capture (SC) take the forms

$$\begin{aligned} P^{\text{SI}} &= \sum_{k=1}^4 P_k^{\text{SI}} = 2 \sum_{k=1}^4 p_k^{\text{ion}} p_k^{\text{el}} \prod_{j \neq k} (p_j^{\text{el}})^2, \\ P^{\text{SC}} &= \sum_{k=1}^4 P_k^{\text{SC}} = 2 \sum_{k=1}^4 p_k^{\text{cap}} p_k^{\text{el}} \prod_{j \neq k} (p_j^{\text{el}})^2. \end{aligned} \quad (6)$$

One alternative to the standard IPM is the IEVM, suggested in Ref. [33] and used in several works (e.g., [34–36]) for ion collisions with He. Following the interpretation of Janev *et al.* [34], the IEVM assumes that the many-electron removal takes place sequentially. For ion- $\text{H}_2\text{O}^+$  collisions, this means that the second electron is removed from  $\text{H}_2\text{O}^+$ . Therefore, the implementation of the IEVM consists of substituting in (6) the elastic probabilities  $p_j^{\text{el}}$  by  $\mathcal{P}_j^{\text{el}}$ , where  $\mathcal{P}_j^{\text{el}} = 1 - \mathcal{P}_j^{\text{ion}} - \mathcal{P}_j^{\text{cap}}$  and  $\mathcal{P}_j^{\text{ion, cap}}$  are one-electron probabilities calculated for ion- $\text{H}_2\text{O}^+$  collisions. However, previous calculations for ion- $\text{H}_2$  collisions [42] indicate that the electrons on the same shell are equivalent, and accordingly, we have not distinguished between ionization and capture probabilities for electrons on the same shell; this leads to

$$\begin{aligned} P^{\text{SI}} &= \sum_{k=1}^4 P_k^{\text{SI}} = 2 \sum_{k=1}^4 p_k^{\text{ion}} p_k^{\text{el}} \prod_{j \neq k} (\mathcal{P}_j^{\text{el}})^2, \\ P^{\text{SC}} &= \sum_{k=1}^4 P_k^{\text{SC}} = 2 \sum_{k=1}^4 p_k^{\text{cap}} p_k^{\text{el}} \prod_{j \neq k} (\mathcal{P}_j^{\text{el}})^2. \end{aligned} \quad (7)$$

These formulas can be further simplified by taking into account that  $\mathcal{P}_j^{\text{ion, cap}}$  are small because they involve electron removal from a positive ion, so that  $\mathcal{P}_j^{\text{el}} \approx 1$ . We have employed this simplification in the present calculations, yielding

$$\begin{aligned} P^{\text{SI}} &= 2 \sum_{k=1}^4 p_k^{\text{ion}} p_k^{\text{el}}, \\ P^{\text{SC}} &= 2 \sum_{k=1}^4 p_k^{\text{cap}} p_k^{\text{el}}. \end{aligned} \quad (8)$$

It is well known that processes involving the removal of more than one electron are, in general, not well described in the framework of the IPM. In this respect, we have found, taking experimental data on  $\text{H}^+ + \text{H}_2\text{O}$  collisions as references, that both single- and double-electron processes are better described by our implementation of the IEVM (see, however, [36,43]). The probabilities for transfer ionization

(TI), double ionization (DI), and double capture (DC) are obtained following arguments similar to those leading to (8):

$$\begin{aligned} P^{\text{TI}} &= 2 \sum_{k=1}^4 p_k^{\text{ion}} p_k^{\text{cap}}, \\ P^{\text{DI}} &= \sum_{k=1}^4 (p_k^{\text{ion}})^2, \\ P^{\text{DC}} &= \sum_{k=1}^4 (p_k^{\text{cap}})^2. \end{aligned} \quad (9)$$

Finally, in order to compare our ionization cross sections with the available experimental data as well as to other theoretical predictions, it is useful to define the probability of electron production (EP) (or *net* ionization),  $P^{\text{EP}}$ , as

$$P^{\text{EP}} = P^{\text{SI}} + 2P^{\text{DI}} + P^{\text{TI}} = 2 \sum_{k=1}^4 p_k^{\text{ion}} \quad (10)$$

and, in a similar way, to define the *net* capture probability as

$$P_{\text{net}}^{\text{C}} = P^{\text{SC}} + 2P^{\text{DC}} + P^{\text{TI}} = 2 \sum_{k=1}^4 p_k^{\text{cap}}, \quad (11)$$

where we have neglected the probabilities for three-electron processes.

### C. Anisotropy and orientation-averaged cross sections

The available experimental data correspond to ion collisions with gas-phase targets; it is therefore necessary to average the calculated cross sections over the molecule orientation to compare with them. In this respect, anisotropy effects should be washed out, to some extent, when averages over both projectile-target relative orientations and the four MOs involved are performed to mimic nonaligned experimental conditions. The orientation average can be carried out in an equivalent way by averaging over the direction of the projectile velocity, keeping the molecule orientation fixed in the laboratory reference frame. Explicitly,

$$\sigma^X(v) = \frac{1}{4\pi} \int d\mathbf{b} \int d\Omega P^X(\mathbf{b}, v, \Omega), \quad (12)$$

where  $\Omega$  is the solid angle that defines the direction of  $\mathbf{v}$  and  $X = \text{SI, SC, TI, DI, or EP}$ . The integration has been performed numerically by applying the method of Ref. [44], where the integral over  $d\Omega$  is obtained by means of a six-point Newton-Côtes formula. The integration over  $d\mathbf{b}$  is then carried out with the restriction  $\mathbf{b} \perp \mathbf{v}$ , and we have considered four orientations of the impact parameter  $\mathbf{b}$  in the plane perpendicular to each orientation of  $\mathbf{v}$ . Finally, taking into account the molecular symmetry, the orientation-averaged cross section is given by a combination of cross sections calculated for the 10 projectile trajectories illustrated in Fig. 3:

$$\sigma^X(v) = \frac{1}{12} \left( \sum_{m=1}^{10} \sigma_m^X + \sigma_4^X + \sigma_8^X \right), \quad (13)$$



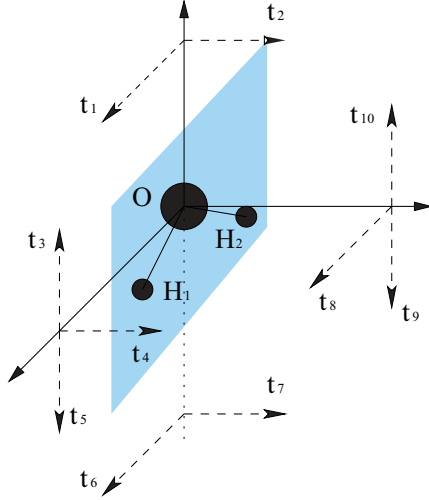


FIG. 3. (Color online) Ion trajectories employed in the orientation average.

with

$$\sigma_m^X = 2\pi \int_0^\infty b P_m^X(b, v) db. \quad (14)$$

The probabilities  $P_m^X$  have been evaluated for nuclear trajectories with the orientation  $t_m$  (see Fig. 3).

### III. H<sup>+</sup> + H<sub>2</sub>O COLLISIONS

In this section, we compare our total cross sections to different experimental and theoretical results for the H<sup>+</sup> + H<sub>2</sub>O system in the energy range  $20 \text{ keV} \leq E \leq 10 \text{ MeV}$ . In Fig. 4(a), we compare our cross sections for SI with perturbative CDW [19,20] and FB [21] calculations and experiments [12–14]. Our present calculations, which use the three-center model potential and the IEVM, lead to cross sections in better agreement with the experimental ones than our previous CTMC calculations in Ref. [22], which employed a  $Z_{\text{eff}}$  description of the target and the IPM. Moreover, at high energies our SI cross section shows an energy dependence similar to that of the CDWEIS [19,20] and FB [21] calculations.

The total cross sections for EP are obtained by integrating the probabilities of Eq. (10) over the impact parameter, and in Fig. 4(b), we compare the experimental data of Refs. [45] and [46] with the theoretical data of Ref. [26], issued from BGM calculations. We have also included in Fig. 4(b) the data of Ref. [14] for  $E < 100 \text{ keV/amu}$ , which, as explained by the authors, is the sum of SI and TI cross sections; indeed, double ionization is expected to be very small at low  $E$ , so the EP cross section must be practically identical to the sum of the SI and TI ones. Our improved CTMC results are in very good agreement with all measurements. They also nicely agree with the BGM results of Ref. [26], even though the maximum of the CTMC is located at slightly higher  $E$  than its BGM counterpart.

Our orientation-averaged SC cross section  $\sigma^{\text{SC}}$  is displayed in Fig. 5(a) as a function of the impact energy  $E$ . Figure 5 also

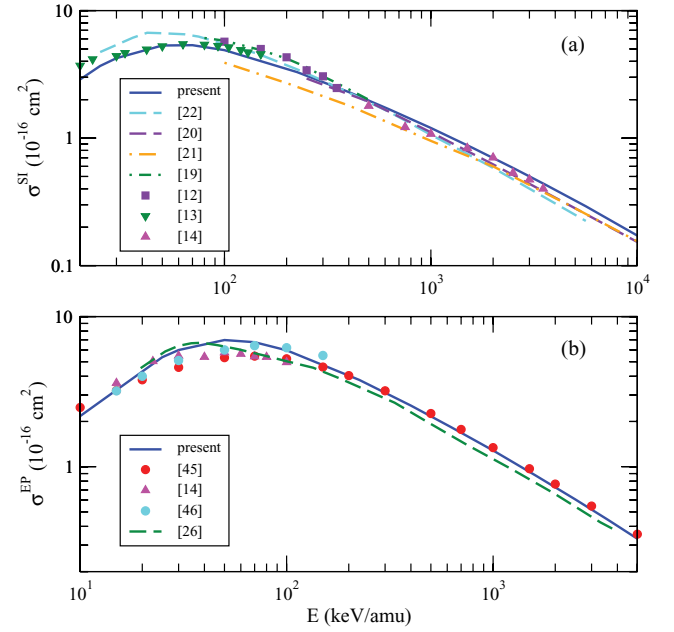


FIG. 4. (Color online) Total cross sections for (a) single ionization,  $\sigma^{\text{SI}}$ , and (b) electron production,  $\sigma^{\text{EP}}$ , in proton collisions with water as functions of the collision energy. The present calculations are compared with previous calculations and experiments.

includes the experimental data of Refs. [13,14,47] as well as our previous CTMC calculations using  $Z_{\text{eff}}$  and IPM [22]. The improvement inherent in the use of the three-center  $V_{\text{mod}}$  and the IEVM clearly shows up as one compares our previous and present CTMC results, taking into account that the latter ones nicely agree with experiments over the whole impact energy range. Our computed *net* capture cross section, displayed in

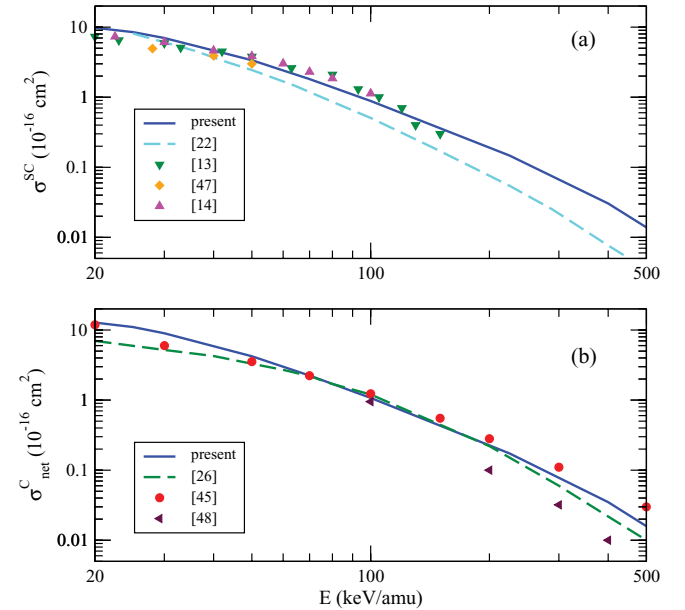


FIG. 5. (Color online) Total cross sections for (a) single-electron capture,  $\sigma^{\text{SC}}$ , and (b) net electron capture,  $\sigma_{\text{net}}^{\text{C}}$ , in proton collisions with water as functions of collision energy. The present calculations are compared with previous calculations and experiments.

Fig. 5(b), is also in agreement with both the measurements [45,48] and BGM calculations [26]. The present CTMC and BGM descriptions use an adequate anisotropic description of the target, so that the small deviations that persist between the corresponding sets of results are attributed to the liabilities of both IPM and IEVM to provide very accurate cross sections for two electron processes; here the TI contribution to *net* capture has been found to be one order of magnitude smaller than the SC contribution for  $E > 50$  keV/amu, but it can be slightly overestimated at lower  $E$ .

We now turn our attention to the sensitivity of SI and SC cross sections and probabilities to relative projectile-target orientations (i.e., to anisotropy). In Fig. 6(a) we present the SI cross sections computed according to (14) for some representative nuclear orientations. For SI as well as for SC, we have found that different orientations lead to similar cross sections over the whole  $10 \text{ keV} < E < 10 \text{ MeV}$  impact energy range. In particular,

$$\begin{aligned}\sigma_1^{\text{SC,SI}} &\approx \sigma_2^{\text{SC,SI}}, \\ \sigma_3^{\text{SC,SI}} &\approx \sigma_5^{\text{SC,SI}}, \\ \sigma_8^{\text{SC,SI}} &\approx \sigma_9^{\text{SC,SI}} \approx \sigma_{10}^{\text{SC,SI}}.\end{aligned}\quad (15)$$

Accordingly, we present in Fig. 6(a) the SI cross sections as functions of  $E$  for six trajectory orientations,  $t_1$ ,  $t_3$ ,  $t_4$ ,  $t_6$ ,  $t_7$ , and  $t_8$  (see Fig. 3), together with the averaged cross section  $\sigma^{\text{SI}}$  of (13). The relations  $\sigma_6^{\text{SI}} > \sigma_3^{\text{SI}} > \sigma_7^{\text{SI}} > \sigma_4^{\text{SI}} > \sigma_8^{\text{SI}} > \sigma_1^{\text{SI}}$  and  $\sigma_4^{\text{SI}} \approx \sigma^{\text{SI}}$  are generally fulfilled for the range of energies studied. The relative magnitudes of the cross sections can be easily understood with the help of Figs. 1 and 2: trajectories  $t_6$  and  $t_{3,5}$  take place in the molecular plane, where the electron density is maximum for the  $2a_1$ ,  $3a_1$ , and  $1b_2$  MOs;  $t_6$  passes close to both H atoms, whereas  $t_3$  and  $t_5$  graze only one of these two centers, from which follows  $\sigma_6^{\text{SI}} > \sigma_{3,5}^{\text{SI}}$ . Trajectories

$t_4$  and  $t_7$  correspond to projectile trajectories perpendicular to the molecular plane; such an orientation favors transitions from the  $1b_1$  MO but makes the transitions from the three inner MOs smaller. Therefore,  $\sigma_{3,5,6}^{\text{SI}} > \sigma_{4,7}^{\text{SI}}$  and  $\sigma_7^{\text{SI}} > \sigma_4^{\text{SI}}$  since  $t_7$  passes in between the two H atoms, while  $t_4$  feels only one of them. Trajectories  $t_8$ ,  $t_9$ , and  $t_{10}$  are out-of-plane trajectories; all of them cross regions of lower electron densities and are, accordingly, amenable to smaller ionizing transitions than the previous groups of trajectories. Finally,  $t_1$  and  $t_2$  mostly graze the O nucleus that deeply retains electrons and therefore minimizes electron removal.

The ordering of SI cross sections with respect to the projectile-target orientations also holds for SC cross sections at  $E < 200$  keV/amu, but we find that  $\sigma_4^{\text{SC}}$  is the lowest cross section at  $E > 200$  keV/amu [see Fig. 6(b)]. The overall similitude of SC and SI behaviors indicates that the trajectory orientation mainly determines the amplitude of electron removal from the target.

We present in Fig. 7, as functions of  $b$ , the weighted mono-electronic ionization ( $bp_k^{\text{ion}}$ ) and capture ( $bp_k^{\text{cap}}$ ) probabilities for the  $t_4$  projectile-target orientation, which is such that  $\sigma_4^{\text{SI}} \approx \sigma^{\text{SI}}$ , for each initial valence MO  $\phi_i$ . We plot these probabilities for  $v = 1$  and 2 a.u. The former impact velocity roughly corresponds to the maximum of the averaged SI cross section [see Fig. 6(a)], where ionization and capture strongly compete with each other;  $v = 2$  a.u. is representative of the high-velocity regime, and we have explicitly checked that the trends observed in Fig. 7 at  $v = 2$  a.u. hold for higher  $v$ . We have also verified that  $t_m$  trajectories with  $m \neq 4$  lead to similar features to those displayed in Fig. 7.

Concerning ionization, we observe that the more weakly bound the MO is, the larger the corresponding  $p_i^{\text{ion}}$  is; this conforms to our intuition as well as to our experience in ion-atom collisions, where it is well known that it is generally

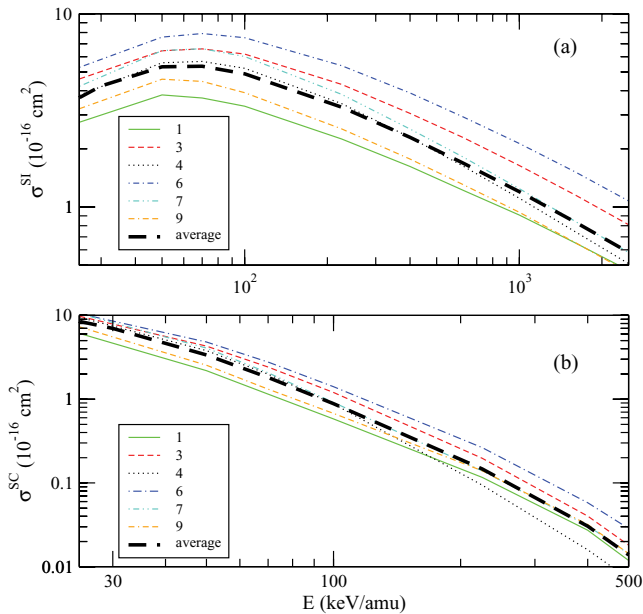


FIG. 6. (Color online) (a) Single-ionization and (b) single-capture cross sections as a function of the impact energy for  $\text{H}^+ + \text{H}_2\text{O}$  collisions for the trajectory orientations of Fig. 3.

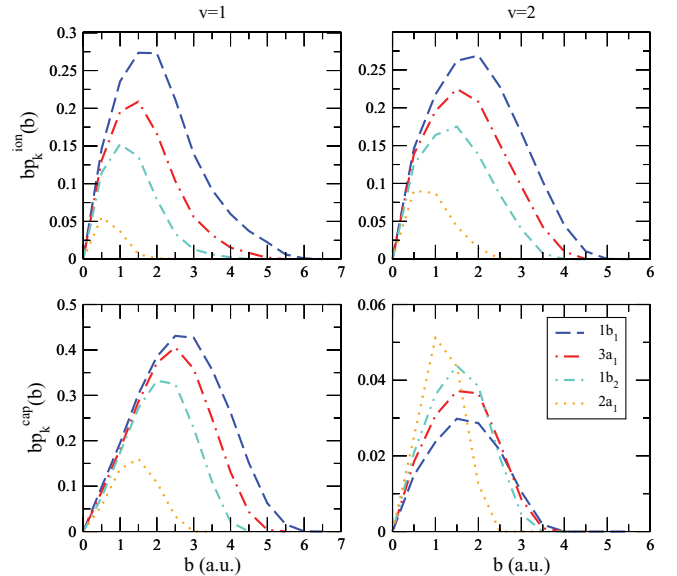


FIG. 7. (Color online) One-electron transition probabilities for (top) ionization  $p_k^{\text{ion}}$  and (bottom) capture  $p_k^{\text{cap}}$ , multiplied by the impact parameter  $b$ , as functions of  $b$  for  $\text{H}^+ + \text{H}_2\text{O}$  collisions at (left)  $v = 1$  a.u. and (right)  $v = 2$  a.u. and for the trajectory orientation described in the text.

easier to pull out an electron from a highly excited orbital. Furthermore, the weighted probabilities  $bp_i^{\text{ion}}$  peak at larger  $b$  when the initial MO is more diffuse; once again, such a behavior is intuitive and can be traced back to the spatial extension of the MO. The capture probabilities  $bp_i^{\text{cap}}$  behave as their ionization counterparts at small  $v$ ; in this velocity regime, the first steps of ionization and capture mechanisms are the same [49–51], so that it is reasonable to obtain similar trends for capture and ionization as a function of  $b$ . As  $v$  increases, we find that the contribution to the electron capture of the inner MO,  $2a_1$ , increases, becoming the the main contribution for  $v > 2.0$  a.u. ( $E > 100$  keV/amu). In fact, electron capture occurs at small impact parameters, where inner-shell processes are also known to be important in ion-atom systems.

#### IV. He<sup>2+</sup> + H<sub>2</sub>O COLLISIONS

Our cross section for electron production is compared in Fig. 8 with the experimental data of Refs. [52–54], as a function of the impact energy  $E$ . Good agreement is found for  $E \geq 50$  keV/amu, but discrepancies appear at lower  $E$ , where the underestimation of the experimental EP cross section can be attributed to the inaccurate computation, by means of the IEVM, of the many-electron probabilities that contribute to EP. On the other hand, the SI cross section, included in Fig. 8, largely falls down as  $E$  decreases from 50 to 10 keV/amu. In addition to IEVM liabilities, at low  $E$ , the SI contribution to EP can be underestimated due to the use of microcanonical phase-space initial conditions in the CTMC calculations; such a problem is widely documented for low- $E$  multicharged ion-atom collisions [55,56]: in these (simple) collisional systems, it was soon realized [55] that accurate calculations of inelastic cross sections at low and intermediate  $E$  require the use of improved initial conditions, beyond the microcanonical framework. Such improved initial conditions involve an electron energy distribution that spreads over the entire energy bin associated with the entry channel [57] and therefore allow us to mimic, to some extent, under-barrier

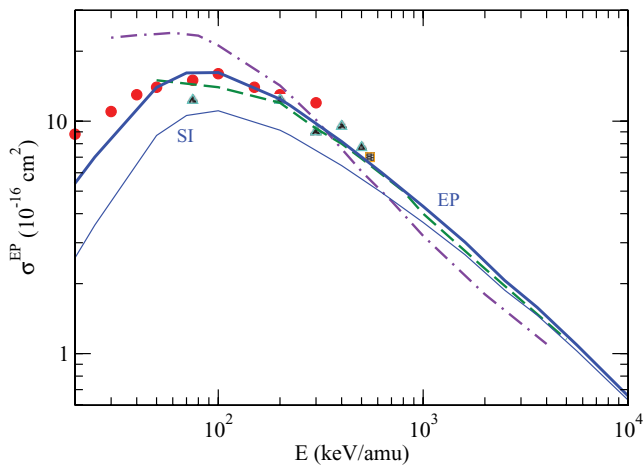


FIG. 8. (Color online) Electron production cross sections as a function of the impact energy for He<sup>2+</sup> + H<sub>2</sub>O collisions. Present calculations: blue solid lines. Theoretical results: green dashed line, [27]; purple dot-dashed line, [28]. Experimental results for EP: circles, [52]; triangles, [53]; squares, [54].

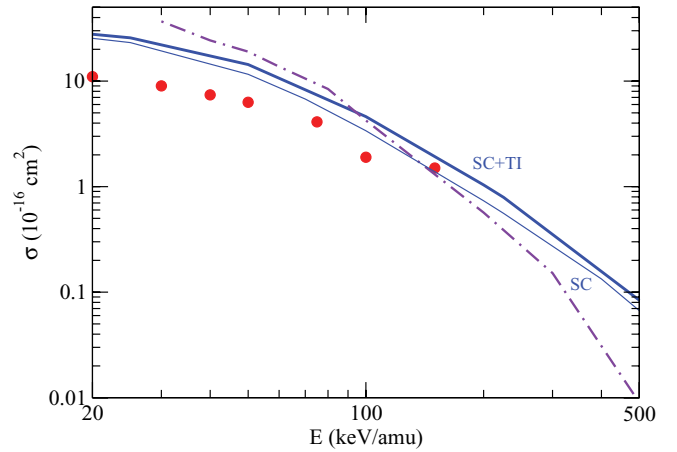


FIG. 9. (Color online) Single capture plus transfer ionization (SC + TI) cross sections for He<sup>2+</sup> + H<sub>2</sub>O collisions as a function of the impact energy: present results, blue solid lines; classical calculations, purple dot-dashed line (from [28]); experimental data, circles (from [52]).

transitions, which are significant for projectile charges  $Z_P \neq 1$ . In this respect, the over-barrier-based model of Ref. [28], which does not account for target anisotropy, works worse than the present CTMC approach at any  $E$ . The FB calculations [27] behaves better at  $E \geq 200$  keV/amu and coalesce, in this energy range, with the present CTMC EP cross section.

Since SC total cross sections have so far not been measured for He<sup>2+</sup> impact, we plot in Fig. 9 the sum of SC and TI cross sections as a function of  $E$  and compare them with the measurements of Rudd *et al.* [52] and over-barrier calculations of Abbas *et al.* [28]. The shape of the experimental cross section is well reproduced by our calculations; nevertheless, the measured and computed cross sections differ in magnitude (up to a factor of  $\sim 2$  at low  $E$ ). The TI contribution to the SC + TI cross section is found to be small over the whole impact energy range since  $\sigma_{\text{SC}} \approx \sigma_{\text{SC}} + \sigma_{\text{TI}}$  in Fig. 9. The over-barrier model [28] does not allow us to ascertain either the experimental or the present CTMC-IEVM values of the SC + TI cross section since it yields a badly shaped cross section. Given the similar shape of the experimental and CTMC cross sections and the fact that improved calculations should safely lead to larger cross sections at low and intermediate energies, new experimental investigations of both SC and TI cross sections are desirable. This would allow us to elicit, together with implementation of improved calculations, the validity and limitations of the IEVM at low  $E$ .

#### V. C<sup>6+</sup> + H<sub>2</sub>O COLLISIONS

Drawing from the satisfactory implementations of the three-center CTMC model for H<sup>+</sup> and He<sup>2+</sup> + H<sub>2</sub>O collisions, we have also considered C<sup>6+</sup> ion impact because of its paramount importance in ion-beam cancer therapy. In Fig. 10, we report our computed EP and SI cross sections as functions of  $E$ , lying in the wide range  $10 \text{ keV/amu} \leq E \leq 10 \text{ MeV/amu}$ . Perturbative calculations by Bernal and Liendo [29] and Dal Cappello *et al.* [30] are also included in Fig. 10. It is clear that

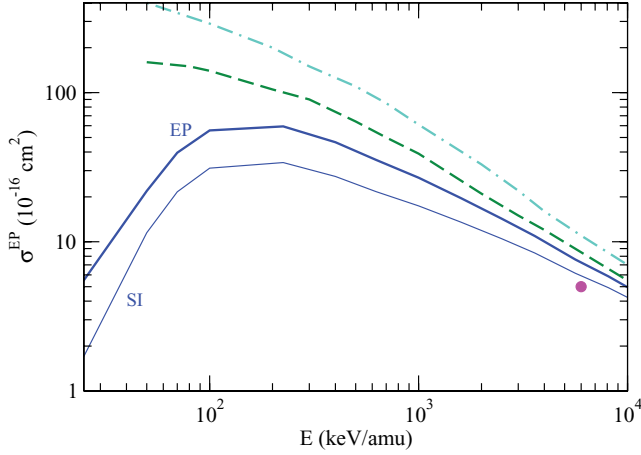


FIG. 10. (Color online) Electron production cross section as a function of the impact energy for  $C^{6+} + H_2O$  collisions. Present calculations for EP and SI, blue solid lines. Electron production from other calculations: light blue dot-dashed line, [29]; green dashed line, [30]. The dot shows the experimental point at  $E = 6$  MeV/amu [30].

present CTMC and perturbative cross sections shall coalesce for  $E > 10$  MeV/amu. In this respect, it has to be noted that the lower bound of validity of perturbative calculations increases with the projectile charge [58], so particular care has to be taken before including perturbative cross sections in the Monte Carlo track structure codes that aim at describing the dynamics induced by charged particles passing through biological environments [15,16]. We safely venture that our nonperturbative CTMC results are more accurate than those of Refs. [29,30]; the former results lie closer to the unique experimental point at  $E = 6$  MeV/amu than the latter ones.

In Fig. 11, we plot our SC and SC + TI cross sections as functions of  $E$ . As for  $He^{2+}$  collisions, we expect that the main limitation of our calculations is the inaccurate treatment of two- and three-electron processes by means of the IEVM, although the estimate of  $\sigma^{TI}$  from Fig. 11 indicates that this process is probably not very relevant at the lowest energies of our calculations.

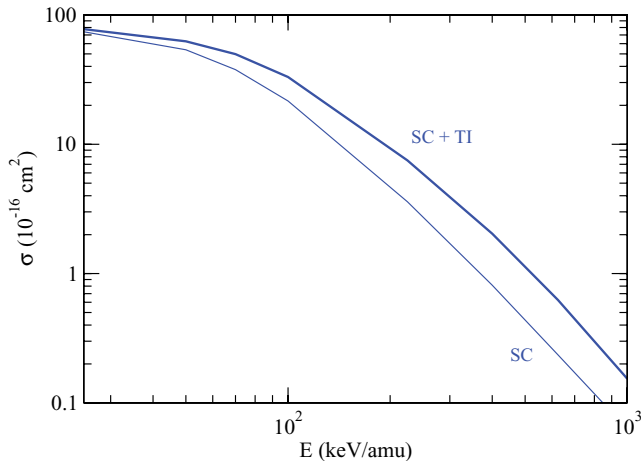


FIG. 11. (Color online) SC + TI and SC cross sections for  $C^{6+} + H_2O$  collisions as functions of the impact energy.

## VI. SCALING LAWS AND FRAGMENTATION

As stated in the Introduction, the collisional database required to model radiation damage and the interaction of charged particles with a biological environment is huge. In this respect, our explicit calculations of cross sections for three ion- $H_2O$  systems can be used to extract some scaling laws, with respect to projectile charge and impact energies, that would avoid the need for further ion- $H_2O$  calculations. We additionally consider in this section the fragmentation processes subsequent to the primary ion- $H_2O$  collisions since heavy fragments are important sources of radiation damage.

### A. Scaling laws for ion- $H_2O$ collisions

Most of the scaling laws that have been derived in atomic collisions stem from first-order perturbative calculations of inelastic cross sections. For instance, FB theory indicates that ionization cross sections behave, in the high velocity regime, as  $Z_p^2 \ln(E)/E$ , whereas, for capture, cross sections scale as  $Z_p^5/v^{12}$  [38]. These scaling relations are valid, and useful, provided the requirements for first-order perturbative conditions are fulfilled. In this respect, the perturbation strength  $Z_p/v$  is the important parameter, and FB (and related laws) apply provided  $Z_p/v \ll 1$ .

At the energy range considered in this work and in the usual radiation damage applications, the FB validity criterion is not fulfilled for high projectile charges. As an example, the previous scaling laws are expected to fail for  $C^{6+}$  impact if  $E < 1$  MeV/amu, where term orders higher than 1 are necessary, within perturbative expansions, to account for strong interactions between target and projectile. Introducing high-order terms in Born-type expansions is generally not a practical solution to derive simple scaling laws (nonunitarity problems can also show up), and nonperturbative calculations hide simple relations between cross sections,  $Z_p$  and  $v$ . One is thus led to derive semiempirical relations *a posteriori* from calculations involving various  $Z_p$  and  $v$  for a given target.

Such explicit calculations in ion-atom collisions [59,60] have shown that ionization cross sections fall in a universal curve, in both the  $Z_p/v < 1$  and  $Z_p/v > 1$  regimes, if the cross section and the impact energy are linearly scaled with  $Z_p$ . In this work, we show in Fig. 12 that the same applies for EP cross sections for  $E/Z_p \geq 100$  keV/amu, where  $\sigma^{EP} \approx \sigma^{SI}$ . The relation between  $\sigma^{EP}/Z_p$  and  $E/Z_p$  must not be confused with the usual Born scaling; it also allows us to reproduce the strong interaction effects on the cross section when  $v < Z_p$ .

Concerning electron capture, we show in Fig. 13 that, for  $E$  ranging from  $\sim 100$  keV/amu to  $\sim 1$  MeV/amu, SC cross sections for multicharged ion impact can be simply, and quite accurately, scaled using  $H^+$  reference data through  $\sigma^{SC}(Z_p, v) = Z_p^2 \sigma^{SC}(1, v)$ . The latter relation is in sharp disagreement with the FB capture scaling that would apply for  $E \gg 1$  MeV/amu. For energies lower than 100 keV/amu, it seems that a linear scaling with respect to  $Z_p$  is better than the proposed  $Z_p^2$  one (see Fig. 13); this agrees with the low- $E$  over-barrier prediction of Knudsen *et al.* [61], which leads to constant  $\sigma^{SC}(Z_p, v)/Z_p$  values for any values of  $Z_p$  and  $v$ . In other words, our proposed SC scaling fills the gap between the low- and high-velocity regimes.



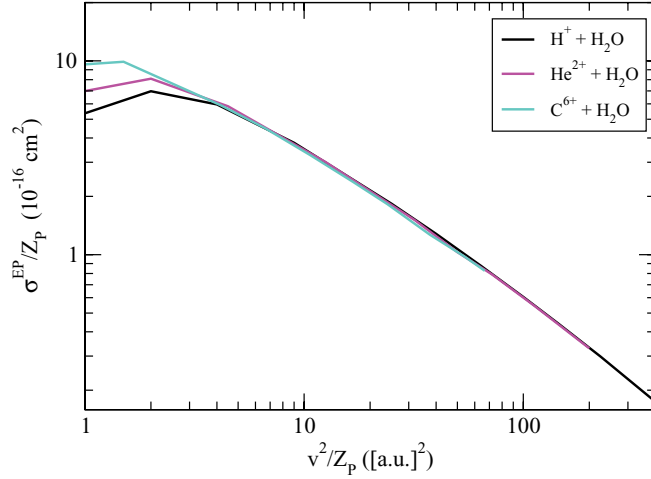


FIG. 12. (Color online) Electron production cross sections over  $Z_p$  as a function of  $v^2/Z_p$  for  $H^+$ ,  $He^{2+}$ , and  $C^{6+} + H_2O$  collisions.

Finally, the scaling relations that apply to bare projectile impact can be safely used for dressed projectiles at intermediate  $E$  when inner electronic structure is not important [38,62].

### B. Fragmentation cross sections

Fragmentation reactions are of great importance in the radiation damage of biological systems by ion impact (see [63]) because the secondary ions formed in the fragmentation can interact with DNA. In this work, we focus on the fragmentation processes associated with the most significant SC and SI (single) electron removals. Indeed, SC and SI can occur throughout a nondissociative process, leading to a stable  $H_2O^+$  fragment, and also through dissociative pathways. Under the assumption that dissociation takes place after the electron transitions [14,19,65], the dissociation channels consist of (i) evaporation  $H_2O^+ \rightarrow OH^+ + H$ , (ii) fission  $H_2O^+ \rightarrow OH + H^+$ , and (iii) breakup  $H_2O^+ \rightarrow O^+ + H + H$ . The cross sections associated with all these channels are computed by multiplying the branching ratios of Tan *et al.* [66], for fragmentation subsequent to electron removal

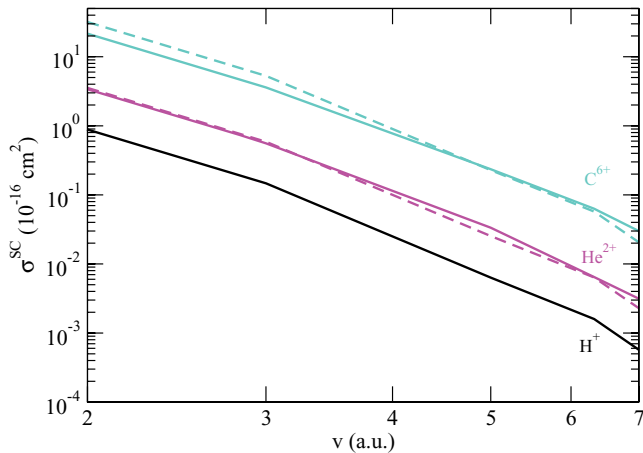


FIG. 13. (Color online) Single-capture cross sections as a function of the collision velocity for  $H^+$ ,  $He^{2+}$ , and  $C^{6+} + H_2O$  collisions. Dashed lines show proton data multiplied by  $Z_p^2$ .

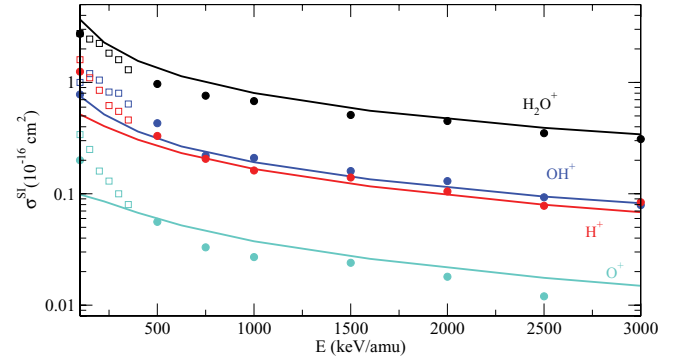


FIG. 14. (Color online) Cross sections for the formation of  $H_2O^+$ ,  $OH^+$ ,  $H^+$ , and  $O^+$  fragments after single ionization in  $H^+ + H_2O$  collisions. Lines, our calculations; squares, experimental data of Werner *et al.* [12]; circles, experimental data of Luna *et al.* [14].

from identified  $H_2O$  MOs, by our previously computed MO-resolved SC and SI cross sections:

$$\begin{aligned} \sigma_{H_2O^+}^{SC,SI} &= 1.00 \sigma^{SC,SI}(1b_1) + 1.00 \sigma^{SC,SI}(3a_1) \\ &\quad + 0.08 \sigma^{SC,SI}(1b_2), \\ \sigma_{OH^+}^{SC,SI} &= 0.70 \sigma^{SC,SI}(1b_2), \\ \sigma_{H^+}^{SC,SI} &= 0.22 \sigma^{SC,SI}(1b_2) + 0.74 \sigma^{SC,SI}(2a_1), \\ \sigma_{O^+}^{SC,SI} &= 0.26 \sigma^{SC,SI}(2a_1). \end{aligned} \quad (16)$$

In practice, the fragmentation cross sections have only been computed for  $H^+$  impact; for other projectile charges, the fragmentation cross sections can easily be derived using (16) and the scaling relations for SC and SI cross sections previously discussed.

In Fig. 14 we report the fragmentation cross sections after SI in the  $150 \leq E \leq 3000$  keV/amu impact energy range and compare them to the experimental results of Luna *et al.* [14] and Werner *et al.* [12]. It is worth noting that the later measurements correspond to fragmentation after either SI or TI; nonetheless, the  $\sigma^{TI}$  cross section is largely smaller than the  $\sigma^{SI}$  one in the energy range considered. It can be seen in Fig. 14 that our fragmentation cross sections are in close agreement with experiments for  $E \geq 400$  keV, but significant discrepancies appear at lower  $E$ . These discrepancies cannot be attributed to the assumption of fragmentation delayed with respect to electron removal since it safely applies in the  $E \geq 150$  keV energy range considered in Fig. 14. They may rather stem from an underestimation of the  $\sigma^{SI}(2a_1)$  cross section for  $E \gtrsim 100$  keV due to the use of microcanonical initial conditions for the innermost  $2a_1$  shell, which leads to a less diffuse radial distribution than the corresponding quantal one (see Fig. 1). According to (16),  $\sigma^{SI}(2a_1)$  indeed contributes to the fission ( $\sigma_{H^+}^{SI}$ ) and breakup ( $\sigma_{O^+}^{SI}$ ) cross sections, which are underestimated in Fig. 14, while  $\sigma_{H_2O^+}^{SI}$  and  $\sigma_{OH^+}^{SI}$  satisfactorily agree with the data of Luna *et al.* [14] down to  $E = 100$  keV. In this respect, it has to be noted that the fragmentation cross sections provide a more stringent check of the accuracy of the MO-resolved SI cross sections than the total  $\sigma^{SI}$ , to which  $\sigma^{SI}(2a_1)$  contributes little (see Fig. 7).

In Fig. 14, SI is mostly nondissociative regardless of  $E$  is because it is mainly tailored by electron removal from the outer

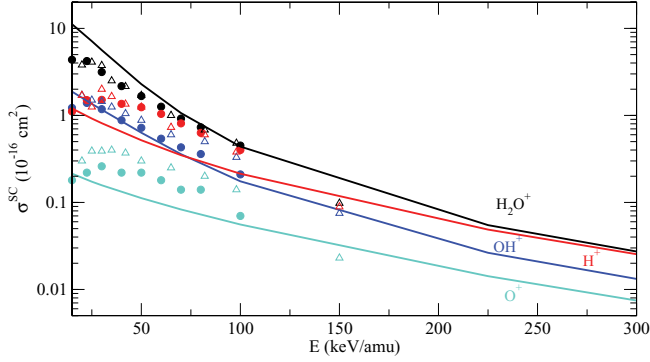


FIG. 15. (Color online) Cross sections for the formation of  $\text{H}_2\text{O}^+$ ,  $\text{OH}^+$ ,  $\text{H}^+$ , and  $\text{O}^+$  fragments after single-electron capture in  $\text{H}^+ + \text{H}_2\text{O}$  collisions. Lines, our calculations; circles, experimental data of Luna *et al.* [14]; triangles, experimental data of Gobet *et al.* [13,64].

$1b_2$ ,  $3a_1$ , and  $1b_1$  MOs (see Fig. 7), which favor the production of stable  $\text{H}_2\text{O}^+$  according to (16). Furthermore, all the product cross sections present parallel shapes as functions of  $E$  for  $E > 100$  keV. As explained by Montenegro *et al.* [67], this pattern shows up in the high-impact-velocity regime where all the MO-resolved SI cross sections exhibit the Bethe-Born  $(1/I_P)\ln(E)/E$  behavior as a function of  $E$ , where  $I_P$  is the ionization potential of the MO, so that, according to (16), the ratios  $\sigma_{\text{H}_2\text{O}^+}^{\text{SI}} : \sigma_{\text{OH}^+}^{\text{SI}} : \sigma_{\text{H}^+}^{\text{SI}} : \sigma_{\text{O}^+}^{\text{SI}}$  reduce to the constant values  $[1/I_P(3a_1) + 1/I_P(1b_1) + 0.08/I_P(1b_2)] : [0.70/I_P(1b_2)] : [0.74/I_P(2a_1) + 0.22/I_P(1b_2)] : [0.26/I_P(2a_1)] = 0.1423 : 0.0368 : 0.0316 : 0.0070$ .

The fragmentation cross sections (16) after single-electron capture are plotted in Fig. 15 for  $E$  lying in the intermediate range 20–300 keV. Our calculations are compared to the experimental data of Luna *et al.* [14] and Gobet *et al.* [64]. As for SI, it seems that our  $\sigma^{\text{SC}}(2a_1)$  cross section is underestimated for  $E \leq 100$  keV, so that the fission ( $\sigma_{\text{H}^+}^{\text{SC}}$ ) and breakup ( $\sigma_{\text{O}^+}^{\text{SC}}$ ) cross sections lie below the measurements, while  $\sigma_{\text{H}_2\text{O}^+}^{\text{SC}}$  and  $\sigma_{\text{OH}^+}^{\text{SC}}$  are in satisfactory agreement with the data of Luna *et al.*

The most conspicuous difference between fragmentation cross sections after SC and those after SI (Figs. 15 and 14, respectively) is that in the former case the lines are not parallel. However, one can note in Fig. 15 that the lines for nondissociative and evaporation reactions and also those for fission and breakup processes are parallel. To explain this fact, one has to take into account that cross sections for fission and breakup reactions are dominated by the contribution of the  $2a_1$  MO, and as explained in Sec. III, the SC probability from this MO increases with  $E$ , becoming clearly dominant at high  $E$ , while a similar effect is not observed in SI. Hence, the energy dependence of  $\sigma^{\text{SC}}(2a_1)$  changes the slope of fission and breakup lines and does not affect the other two lines of Fig. 15. This effect also explains that  $\sigma_{\text{H}^+}^{\text{SC}}$  attains similar values to those of  $\sigma_{\text{H}_2\text{O}^+}^{\text{SC}}$  at high energies.

## VII. CONCLUSIONS

We have employed an improved impact-parameter–CTMC model to calculate cross sections for single-ionization, single-

capture, and two-electron processes (transfer ionization, double capture, and double ionization) in  $\text{H}^+$ ,  $\text{He}^{2+}$ , and  $\text{C}^{6+} + \text{H}_2\text{O}$  collisions in an impact energy range,  $20 \leq E \leq 10\,000$  keV/amu, that largely encompasses the intermediate- and high-energy regimes of interest for ion-based cancer therapy applications. In the framework of the independent-electron approximation, our improved model employs a three-center model potential to describe the interaction of the active electron with the  $\text{H}_2\text{O}^+$  core, beyond the usual one-center  $Z_{\text{eff}}$  description. This has allowed us to explicitly consider anisotropy effects related to the multicenter nature of the target. The evaluation of inelastic probabilities for the physical many-electron system has been performed by means of the IEVM, which has been found to be more accurate than the usual IPM.

For  $\text{H}^+ + \text{H}_2\text{O}$ , our present calculations yield cross sections in better agreement with experiments than previous CTMC calculations that employed a  $Z_{\text{eff}}$  description of the target and the IPM [see Figs. 4(a) and 5(a)], as well as to the BGM results of Lüdde *et al.* [see Figs. 4(b) and 5(b)].

For  $\text{He}^{2+} + \text{H}_2\text{O}$ , the three-center CTMC description provided cross sections in better agreement with the experimental data than the basically over-barrier model of Abbas *et al.* [28] (see Figs. 8 and 9).  $\text{C}^{6+}$  impact has also been considered because of its great importance in ion-beam cancer therapy, in a wide impact-energy range beyond the scope of perturbative approaches (see Figs. 10 and 11).

The explicit calculations of cross sections for the three above-mentioned systems have allowed us to extract some scaling laws, with respect to projectile charge  $Z_P$  and impact energies  $E$ , for electron production and single-capture cross sections (see Figs. 12 and 13). Such scaling laws are useful for filling in the gaps (in  $Z_P$  and  $E$ ) that exist in the collisional database required to model radiation damage and the interaction of charged particles with a biological environment (mainly  $\text{H}_2\text{O}$ ). Finally, we have computed the fragmentation cross sections associated with the single-ionization and single-capture processes (see Figs. 14 and 15). The nondissociative and evaporation ( $\text{H}_2\text{O}^+ \rightarrow \text{OH}^+ + \text{H}$ ) cross sections present satisfactory agreement with measurements from low to high impact energies, whereas the fission ( $\text{H}_2\text{O}^+ \rightarrow \text{OH} + \text{H}^+$ ) and breakup ( $\text{H}_2\text{O}^+ \rightarrow \text{O}^+ + \text{H} + \text{H}$ ) cross sections are underestimated at low  $E$  because of a primary underestimation of the cross sections for electron removal from the innermost  $2a_1$  MO. CTMC calculations beyond the microcanonical framework should allow us to remedy this, similar to what happens in standard ion-atom collisions [57].

The success found in the present application of our multicenter model potential CTMC-IEVM method paves the way for further implementations for other ion-biomolecule collisions.

## ACKNOWLEDGMENTS

This work has been partially supported by the CCG08-UAM/ESP3990 project and the DGICYT project ENE2007-62934.

- [1] U. Amaldi and G. Kraft, *Rep. Prog. Phys.* **68**, 1861 (2005).
- [2] D. Schardt, T. Elsässer, and D. Schulz-Ertner, *Rev. Mod. Phys.* **82**, 383 (2010).
- [3] J. R. Castro, D. E. Linstadt, J.-P. Bahary, P. L. Petti, I. Daftari, J. Collier, P. H. Gutin, G. Gauger, and T. L. Phillips, *Int. J. Radiat. Oncol. Biol. Phys.* **29**, 647 (1994).
- [4] H. Tsujii, S. Morita, T. Miyamoto, J. Mizoe, H. Katou, H. Tsuji, S. Yamada, N. Yamamoto, and H. Murata, in *Progress in Radio-oncology VII* (Monduzzi Editore, Bologna, Italy, 2002), p. 393.
- [5] D. Schulz-Ertner, A. Nikoghosyan, C. Thilmann, T. Haberer, O. Jkel, C. Karger, G. Kraft, M. Wannenmacher, and J. Debus, *Int. J. Radiat. Oncol. Biol. Phys.* **58**, 631 (2004).
- [6] M. Krämer, O. Jäkel, T. Haberer, G. Kraft, D. Schardt, and U. Weber, *Phys. Med. Biol.* **45**, 3299 (2000).
- [7] M. Krämer and M. Scholz, *Phys. Med. Biol.* **45**, 3319 (2000).
- [8] O. Jäkel, G. Hartmann, C. Karger, P. Heeg, and J. Rassow, *Med. Phys.* **27**, 1588 (2000).
- [9] M. Scholz, A. Kellerer, W. Kraft-Weyrather, and G. Kraft, *Radiat. Environ. Biophys.* **36**, 59 (1997).
- [10] J. de Vries, R. Hoekstra, R. Morgenstern, and T. Schlathölter, *Phys. Rev. Lett.* **91**, 053401 (2003).
- [11] B. Boudaïffa, P. Cloutier, D. Hunting, M. A. Huels, and L. Sanche, *Science* **287**, 1658 (2000).
- [12] U. Werner, K. Beckord, J. Becker, and H. O. Lutz, *Phys. Rev. Lett.* **74**, 1962 (1995).
- [13] F. Gobet, S. Eden, B. Coupier, J. Tabet, B. Farizon, M. Farizon, M. J. Gaillard, M. Carré, S. Ouaskit, T. D. Märk *et al.*, *Phys. Rev. A* **70**, 062716 (2004).
- [14] H. Luna, A. L. F. de Barros, J. A. Wyer, S. W. J. Scully, J. Lecointre, P. M. Y. Garcia, G. M. Sigaud, A. C. F. Santos, V. Senthil, M. B. Shah *et al.*, *Phys. Rev. A* **75**, 042711 (2007).
- [15] S. Uehara, L. Toburen, and H. Nikjoo, *Int. J. Radiat. Biol.* **77**, 139 (2001).
- [16] S. Uehara and H. Nikjoo, *J. Phys. Chem. B* **106**, 11051 (2002).
- [17] D. Belkić, *J. Math. Chem.* **47**, 1366 (2010).
- [18] P. D. Fainstein, G. H. Olivera, and R. D. Rivarola, *Nucl. Instrum. Methods Phys. Res., Sect. B* **107**, 19 (1996).
- [19] G. H. Olivera, C. Caraby, P. Jardin, A. Cassimi, L. Adoui, and B. Gervais, *Phys. Med. Biol.* **43**, 2347 (1998).
- [20] B. Gervais, M. Beuve, G. H. Olivera, and M. E. Galassi, *Radiat. Phys. Chem.* **75**, 493 (2006).
- [21] O. Boudrioua, C. Champion, C. Dal Cappello, and Y. V. Popov, *Phys. Rev. A* **75**, 022720 (2007).
- [22] L. F. Errea, C. Illescas, L. Méndez, B. Pons, I. Rabadán, and A. Riera, *Phys. Rev. A* **76**, 040701 (2007).
- [23] J. H. McGuire and L. Weaver, *Phys. Rev. A* **16**, 41 (1977).
- [24] V. Sidorovich, *J. Phys. B* **14**, 4805 (1981).
- [25] H. J. Lüdde and R. M. Dreizler, *J. Phys. B* **18**, 107 (1985).
- [26] H. J. Lüdde, T. Spranger, M. Horbatsch, and T. Kirchner, *Phys. Rev. A* **80**, 060702 (2009).
- [27] C. Champion, O. Boudrioua, C. Dal Cappello, Y. Sato, and D. Ohsawa, *Phys. Rev. A* **75**, 032724 (2007).
- [28] I. Abbas, C. Champion, B. Zarour, B. Lasri, and J. Hassen, *Phys. Med. Biol.* **53**, N41 (2008).
- [29] M. A. Bernal and J. A. Liendo, *Nucl. Instrum. Methods Phys. Res., Sect. B* **262**, 1 (2007).
- [30] C. Dal Cappello, C. Champion, O. Boudrioua, H. Lekadir, Y. Sato, and D. Ohsawa, *Nucl. Instrum. Methods Phys. Res., Sect. B* **267**, 781 (2009).
- [31] L. Méndez, L. F. Errea, C. Illescas, I. Rabadán, B. Pons, and A. Riera, in *Radiation Damage in Biomolecular Systems: Proceedings of the 5th International Conference (RADAM 2008)*, AIP Conf. Proc. No. 1080 (AIP, Melville, NY, 2008), p. 51.
- [32] C. Champion and R. D. Rivarola, *Phys. Rev. A* **82**, 042704 (2010).
- [33] D. S. F. Crothers and R. McCarroll, *J. Phys. B* **20**, 2835 (1987).
- [34] R. K. Janev, E. A. Solov'ev, and D. Jakimovski, *J. Phys. B* **28**, L615 (1995).
- [35] L. A. Wehrman, A. L. Ford, and J. F. Reading, *J. Phys. B* **29**, 5831 (1996).
- [36] J. Bradley, R. J. S. Lee, M. McCartney, and D. S. F. Crothers, *J. Phys. B* **37**, 3723 (2004).
- [37] H. Getahun, L. F. Errea, C. Illescas, L. Méndez, and I. Rabadán, *Eur. J. Phys. D* **60**, 45 (2010).
- [38] B. H. Bransden and M. H. C. McDowell, *Charge Exchange and the Theory of Ion-Atom Collisions* (Clarendon, Oxford, 1992).
- [39] I. Rabadán, L. F. Errea, P. Martínez, and L. Méndez, in *Radiation Damage in Biomolecular Systems: Proceedings of the 5th International Conference (RADAM 2008)*, AIP Conf. Proc. No. 1080 (AIP, Melville, NY, 2008), p. 98.
- [40] R. Abrines and I. C. Percival, *Proc. Phys. Soc.* **88**, 861 (1966).
- [41] C. Illescas, I. Rabadán, and A. Riera, *J. Phys. B* **30**, 1765 (1997).
- [42] D. Elizaga, L. F. Errea, J. D. Gorfinkiel, C. Illescas, L. Méndez, A. Macías, A. Riera, A. Rojas, O. J. Kroneisen, T. Kirchner *et al.*, *J. Phys. B* **32**, 857 (1999).
- [43] A. L. Ford, L. Wehrman, K. A. Hall, and J. F. Reading, *J. Phys. B* **30**, 2889 (1997).
- [44] L. F. Errea, J. D. Gorfinkiel, A. Macías, L. Méndez, and A. Riera, *J. Phys. B* **30**, 3855 (1997).
- [45] M. E. Rudd, T. V. Goffe, R. D. DuBois, and L. H. Toburen, *Phys. Rev. A* **31**, 492 (1985).
- [46] M. A. Bolorizadeh and M. E. Rudd, *Phys. Rev. A* **33**, 888 (1986).
- [47] R. Dagnac, D. Blanc, and D. Molina, *J. Phys. B* **3**, 1239 (1970).
- [48] L. H. Toburen, M. Y. Nakai, and R. A. Langley, *Phys. Rev.* **171**, 114 (1968).
- [49] C. Illescas, I. Rabadán, and A. Riera, *Phys. Rev. A* **57**, 1809 (1998).
- [50] L. F. Errea, C. Harel, C. Illescas, H. Jouin, L. Méndez, B. Pons, and A. Riera, *J. Phys. B* **31**, 3199 (1998).
- [51] E. A. Solov'ev, *J. Phys. B* **38**, R153 (2005).
- [52] M. E. Rudd, T. V. Goffe, and A. Itoh, *Phys. Rev. A* **32**, 2128 (1985).
- [53] L. H. Toburen, W. E. Wilson, and R. J. Popowich, *Radiat. Res.* **82**, 27 (1980).
- [54] P. S. Rudolph and C. E. Melton, *J. Chem. Phys.* **45**, 2227 (1966).
- [55] D. J. W. Hardie and R. E. Olson, *J. Phys. B* **16**, 1983 (1983).
- [56] G. Peach, S. L. Willis, and M. R. C. McDowell, *J. Phys. B* **18**, 3921 (1985).
- [57] L. F. Errea, C. Illescas, L. Méndez, B. Pons, A. Riera, and J. Suárez, *Phys. Rev. A* **70**, 52713 (2004).
- [58] L. F. Errea, L. Méndez, B. Pons, A. Riera, I. Sevilá, and J. Suárez, *Phys. Rev. A* **74**, 012722 (2006).

- [59] A. S. Schlachter, K. H. Berkner, W. G. Graham, R. V. Pyle, P. J. Schneider, K. R. Stalder, J. W. Stearns, J. A. Tanis, and R. E. Olson, [Phys. Rev. A \*\*23\*\*, 2331 \(1981\)](#).
- [60] H. Knudsen, L. H. Andersen, P. Hvelplund, G. Astner, H. Cederquist, H. Danared, L. Liljeby, and K. G. Rensfelt, [J. Phys. B \*\*17\*\*, 3545 \(1984\)](#).
- [61] H. Knudsen, H. K. Haugen, and P. Hvelplund, [Phys. Rev. A \*\*23\*\*, 597 \(1981\)](#).
- [62] C. Illescas and A. Riera, [Phys. Rev. A \*\*60\*\*, 4546 \(1999\)](#).
- [63] N. J. Mason, in *Radiation Damage in Biomolecular Systems: Proceedings of the 5th International Conference (RADAM 2008)*, AIP Conf. Proc. No. 1080 (AIP, Melville, NY, 2008), p. 3.
- [64] F. Gobet, B. Farizon, M. Farizon, M. J. Gaillard, M. Carré, M. Lezius, P. Scheier, and T. D. Märk, [Phys. Rev. Lett. \*\*86\*\*, 3751 \(2001\)](#).
- [65] H. Luna and E. C. Montenegro, [Phys. Rev. Lett. \*\*94\*\*, 043201 \(2005\)](#).
- [66] K. H. Tan, C. E. Brion, P. E. Van der Leeuw, and M. J. Van der Wiel, [Chem. Phys. \*\*29\*\*, 299 \(1978\)](#).
- [67] E. C. Montenegro, S. W. J. Scully, J. A. Wyer, V. Senthil, and M. B. Shah, [J. Electron Spectrosc. Relat. Phenom. \*\*155\*\*, 81 \(2007\)](#).